Effect of DMLS Build Parameters on Defects and Ultrasonic Fatigue Performance of Additively Manufactured AlSi10Mg

Robert K. Rhein[a,*], Qianying Shi[b], Srinivasan Arjun Tekalur[a], J. Wayne Jones[b], Jason W. Carroll[a]

[a] *Eaton Corporation, 26201 Northwestern Highway, Southfield, MI 48076, USA*
[b] *Department of Materials Science and Engineering, University of Michigan, 2300 Hayward Street, Ann Arbor, MI 48109, USA*

Abstract

The high cycle fatigue behavior of additively manufactured AlSi10Mg is evaluated using ultrasonic fatigue as a means to accelerate fatigue testing. Build parameters during the additive manufacturing process are varied and their effect on defect type, size, and distribution is determined. These defects are further found to influence fatigue behavior, which is analyzed using a Murakami $\sqrt{area}$ model. Finally, the ultrasonic fatigue test results are interpreted in the context of applied stress intensity factor and an optimized fatigue limit fit. Two different kinds of physical behavior, representing Murakami dependence and a long crack regime, are found to better correlate the fatigue life behavior than the Murakami model alone. With this information, we can tailor defect size, type, and distribution, within the context of an optimized processing route, to obtain necessary high cycle fatigue properties.

Keywords: additive manufacturing, fatigue, ultrasonic fatigue

1. Introduction

Additive manufacturing (AM) is an attractive technology as it allows for the production of metallic components with relatively complex geometries that can

*Corresponding author
Email address: robrhein@eaton.com (Robert K. Rhein)

be used in a wide array of applications. AM can achieve high resolution and accuracy of component dimensions with minimal loss of base material. Direct metal laser sintering (DMLS) is one kind of powder bed-based AM process that can create metal components by selectively melting powder in a sequential series of layers to fabricate a component according to dimensions specified by slices of a three-dimensional computer aided design (CAD) model.[1] Many different classes of alloy have been produced via DMLS, including Ni-based[2], Ti-based[3,4], and Al-based alloys.[5] Additively manufactured components can have complicated geometries that can be impossible or prohibitively expensive to manufacture using more traditional methods.

Aluminum-silicon alloys are recognized for their corrosion resistance, weldability, and castability and represent approximately 80% of the aluminum casting alloys in use today.[6] In addition, their mechanical properties, high heat conductivity, and low weight make these alloys attractive candidates for automotive and aerospace applications.[7] The binary Al-Si system is eutectic with approximately 12 wt% Si at 577 °C.[8] AlSi10Mg is a traditional cast alloy that is near this eutectic and is often used in AM processes due to its good mechanical properties and weldability.[5]

DMLS parameters have been investigated in order to optimize microstructure and properties in AM AlSi10Mg. DMLS parameters such as beam power and velocity have an influence on the size, type, and distribution of defects in the manufactured component. This in turn influences the static and dynamic mechanical properties of the part. Initial studies focused heavily on the effect of the build parameters on microstructure and porosity on fatigue properties in AM AlSi10Mg. It was shown via single track experiments that a build parameter zone exists between two linear boundaries in power-velocity space that results in an optimized density.[9] It was further demonstrated that the porosity of DMLS-processed AlSi10Mg components is largely governed by the energy density of the laser beam and the hatch spacing used.[10,11] This porosity that arises from manufacturing is a critical variable in determining fatigue performance in an AM material and can never be fully eliminated despite changing

processing conditions and DMLS parameters. Fatigue life depends sensitively on the size and location of the largest of the defects in the population of defects introduced during processing because fatal cracks most often initiate at defects. It is generally accepted that in the presence of defects fatigue lifetime is consumed by crack growth and crack initiation life is negligible. This is consistent with many observations that surface or near-surface defects for equivalent sizes are the most detrimental to fatigue performance.[12,13] Dependence on defect size and location also explains the observed variation in fatigue lifetime, which can be as large as 50%.[14]

When porosity is minimized, the very fine microstructure and distribution of the Si phase in DMLS AlSi10Mg results in hardness, UTS, and elongation properties that are comparable or superior to conventionally cast AlSi10Mg. Mechanical properties can be enhanced via additional heat treatments that result in the precipitation of a $MgSi_2$ phase which significantly strengthens the matrix.[15] It has been shown that AlSi10Mg very high cycle fatigue properties have a strong dependence on the applied heat treatment relative to other build parameters.[16]

Ultrasonic fatigue (USF) testing is a technique that cycles a specimen at very high frequency via resonance, allowing long lifetimes to be reached in a fraction of the time it would take with conventional fatigue testing.[17] This technique, which has been developed for several decades, has been extended to encompass many different testing conditions and has been explicitly used to measure the fatigue properties of DMLS AlSi10Mg.[18]

In the present study a demonstration of the effect that processing parameters have on defect size and distribution within AM AlSi10Mg alloys is sought. It is further shown how the size and type of critical defects present have influence on the overall ultrasonic fatigue performance of these alloys at very long lifetimes.

2. Methodology and Design of Experiment

DMLS AlSi10Mg parts were fabricated on a EOS M290 machine in an argon atmosphere. The EOS machine is equipped with a laser of variable power. Powder particles were sieved and had the composition shown in Table 1.

	Al	Si	Cu	Mn	Mg	Zn	Fe
wt.%	Balance	9-11	<0.05	<0.45	0.45-0.6	<0.1	<0.55

Table 1: Chemical composition of AlSi10Mg powder

A wide range of build parameters were investigated in order to determine their effect on the critical defects present and ultrasonic fatigue performance. A summary of these build parameter permutations is shown in Table 2. Multiple specimens were machined for each set of build conditions. Non-vertical build orientations are taken as relative to the build plane in degrees. 16 mm diameter bars were grown using these build parameters via the DMLS technique.

Specimen ID	Power (W)	Velocity (mm/s)	Layer Thickness (μm)	Hatch Spacing (mm)	Orientation
100-1	220	1000	30	0.16	z
100-2	260	1000	30	0.16	z
100-3	360	1200	30	0.16	z
100-4	340	1000	30	0.16	z
100-5	220	1000	30	0.16	-60
100-6	220	1000	30	0.16	-45
100-7	340	1000	30	0.16	-60
100-8	340	1000	30	0.16	-45
102-1	340	1000	30	0.19	z
102-2	250	600	30	0.19	z
102-3	310	800	30	0.19	z
102-4	250	1400	30	0.19	z
107-1	370	1300	60	0.19	z

107-2	250	600	60	0.19	z
107-3	310	800	60	0.19	z
107-4	340	1100	60	0.19	z
136-1	220	1000	30	0.16	z
136-2	260	1000	30	0.16	z
136-3	360	1200	30	0.16	z
136-4	340	1000	30	0.16	z
136-5	220	1000	30	0.16	-60
136-6	220	1000	30	0.16	-45
136-7	340	1000	30	0.16	-60
136-8	340	1000	30	0.16	-45
136-9	370	1000	30	0.19	z
136-10	250	1600	30	0.19	z

Table 2: Build parameters tested

Build parameters were chosen in some instances to allow direct comparisons between different build sets in order to isolate the effect of particular variables. For example, comparing the builds in the 102-2 (102-3) and 107-2 (107-3) series allows for investigation of the effect of layer thickness. Alternatively, more advanced statistical methods can be employed in order to investigate the combined effect of several build parameters simultaneously.

Ultrasonic fatigue testing equipment used in this study requires the specimen to be designed to resonate at 20 kHz. Specimen dimensions were optimized using a calculation in which the general wave equation was numerically solved by the Newton-Raphson method.[19] Ultrasonic fatigue specimens with a gage section of 5 mm in diameter and 20 mm in length were machined from the as-built cylindrical bars along the vertical build orientation (z) or 60 and 45 degrees relative to the build plane. Specimens were low-stress ground in the final machining step to minimize residual stresses. No heat treatment was performed

prior to testing, leaving the microstructure in the as-built condition. All surface conditions were machined but no additional polishing was conducted.

Following the ultrasonic fatigue testing, fractography by scanning electron microscopy (SEM) was used to identify crack initiation sites. A Tescan Mira-3 scanning electron microscope was used for this characterization. The type, size, and location of critical defects that initiated fatigue failure were identified and measured. In order to estimate the effect of surface and near surface defects which serve as crack initiation sites, the effective size of those defects was defined by the square root of the effective area $\sqrt{area}$, following the method of Murakami et al.[20,21] This effective area depends on the different configurations of initiating defects (shape and location relative to the sample surface), making it larger than the physical projected area of the initiating defect itself. Mechanical properties of specimens in the as-built condition were evaluated by Vickers microhardness. Hardness measurements were obtained on metallographic cross-sections perpendicular to the fatigue specimen axis using a load of 300 g and dwell time of 15 s. Ten hardness measurements were made for each specimen and an average hardness value was calculated.

3. Results

100 vs. 136 series

Taken together, the tests conducted on the 100 and 136 series consider mainly the effect of power and orientation on defects and fatigue behavior. In Figure 1 the build conditions of these two series are plotted in Power-Velocity space following the approach established in[9].

Six distinct power/velocity combinations were tested in the 100 and 136 series combined. In Figure 1, the dashed lines represent bounds of a previously established process window for AlSi10Mg. It is expected from past work that going to higher velocities outside this window will yield lack of fusion defects while lower velocities will yield keyhole defects It is useful to collapse the other build parameter variables into this space because it allows for the relatively

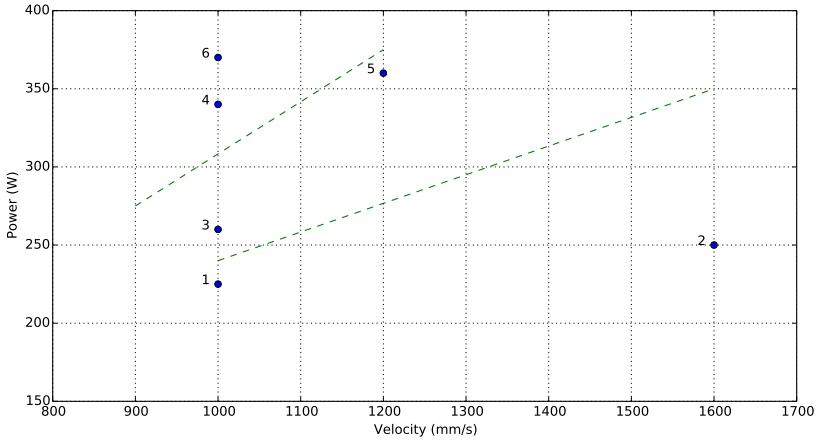

Figure 1: Conditions in the 100 and 136 series plotted in Power-Velocity space. Conditions are labeled in order of increasing power.

simple identification of power/velocity combinations in which a given kind of defect is responsible for fatigue failure during USF testing. The defects that cause this failure will be termed "killer" defects. In this work, all the killer defects in Conditions 2, 3, and 5 were lack of fusion while at least some of the killer defects in Conditions 1, 4, and 6 were of the keyhole type. This is intuitive as employing a higher velocity during DMLS makes it relatively more difficult for powder to fuse, resulting in lack of fusion defects. Representative micrographs contrasting the lack of fusion and keyhole type killer defects are shown in Figure 2.

The distribution of initiating defect sizes for each P-V condition can be represented as a cumulative distribution function (CDF), as shown in Figure 3. The CDF can be defined as:

$$CDF = j * \frac{100}{n+1}(\%) \tag{1}$$

Where j is the relative rank of a defect's size in a given population and n is the total number of initiating defects in that population. The CDF value can therefore be regarded as a probability that a killer defect is a given size

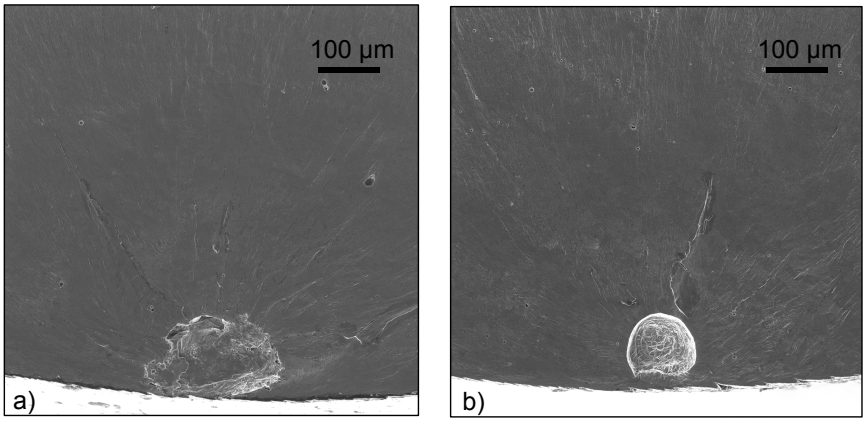

Figure 2: Representative micrographs in the 136 series detailing a) a lack of fusion type killer defect and b) a keyhole type killer defect.

or smaller. Plotted in Figure 3 are the CDFs of the populations labeled 1-6 in Figure 1. Each set of CDF points in Figure 3 represents a population at a distinct power-velocity condition.

As can be seen in Figure 3, the lower power conditions produce larger killer defects. These defects were also characterized as largely a lack of fusion type and the distribution in size is relatively large. The higher power conditions (4-6 in Figure 1) result in smaller defects that have a significantly narrower size distribution. Some of the defects in these higher power populations are keyhole type defects.

Build orientation was not found to play a significant role in the fatigue life of this material, as shown in Figure 4. Likewise, build velocity does not appear to play a significant role in determining defect size or fatigue performance for the build parameter sets considered in the present study. A regression analysis was performed in which it was found that build orientation and velocity have a significantly weaker effect on defect size and fatigue performance than power and layer thickness.

102 vs. 107 series

The effect of layer thickness during DMLS on fatigue performance was also

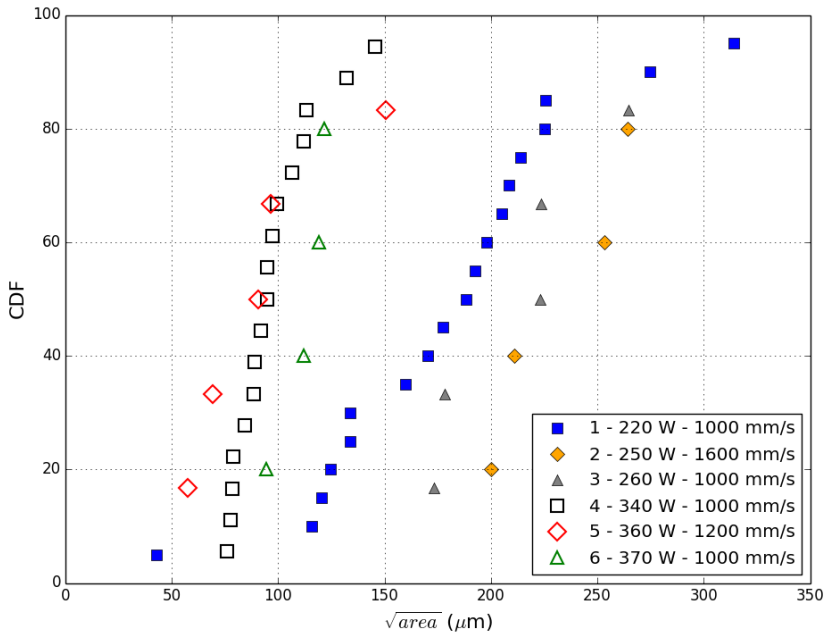

Figure 3: Cumulative distribution plots for the 1-6 Power-Velocity conditions in Figure 1

considered. To this end, two populations of specimens, the 102 and 107 series, were built. The 102 series was fabricated using a 30 μm layer thickness and the 107 series was fabricated using a 60 μm layer thickness. Both the 102 and 107 series considered four different power-velocity conditions each (Table 2), two of which can be directly compared between the series. A plot showing the different power-velocity conditions used in the layer thickness study is shown in Figure 5.

As before, different killer defect sizes and types at the different conditions are observed. If the 250 W/600 mm/s condition is considered, the observed killer defects are almost exclusively of the keyhole type for the 30 μm layer thickness (102 series). For the 60 μm layer thickness in the 107 series the defects are entirely lack of fusion defects. Representative fracture surfaces are shown for

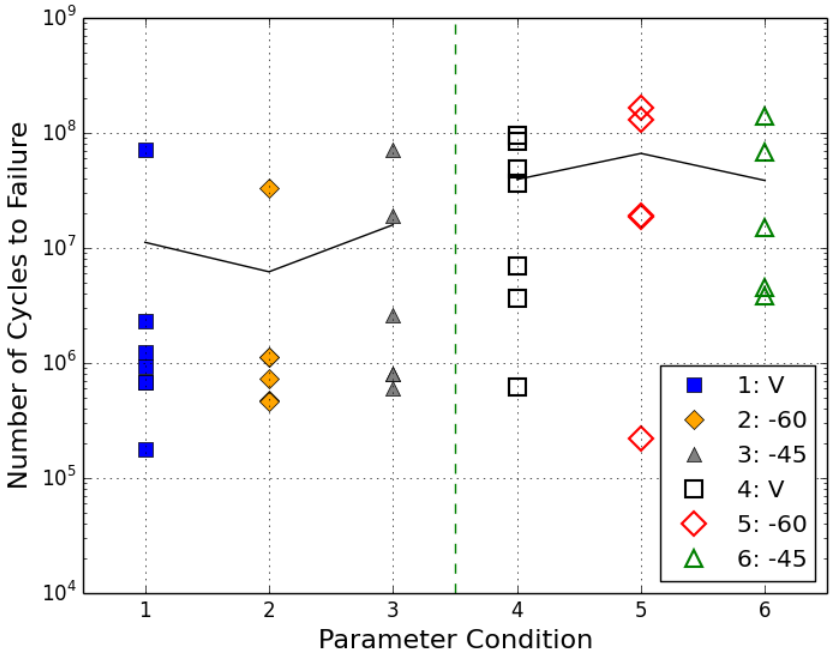

Figure 4: Fatigue life as a function of orientation. Parameter Conditions 1-3 are of different indicated orientations with constant Power = 220 W, Velocity = 1000 mm/s, Layer Thickness = 30 μm, and Hatch Spacing = 0.16 mm. Parameter Conditions 4-6 are of different indicated orientations with constant Power = 340 W, Velocity = 1000 mm/s, Layer Thickness = 30 μm, and Hatch Spacing = 0.16 mm. Number in legend indicates angle in degree from vertical. Black lines connect average fatigue life points between the conditions.

the 102 and 107 series in Figure 6 and it is notable that the keyhole killer defects of the 102 series do not reside on the surface itself. These defects with the distance from the surface smaller than their own equivalent diameter are termed "near surface", which are intermediate in character between surface and interior defects (the distance from the surface is larger than their own equivalent diameter).

The size and distribution of the observed killer defects as a function of layer thickness for the 250 W, 600 mm/s build condition is shown in Figure 7, which shows that the smaller 30 μm layer thickness has a significantly smaller average

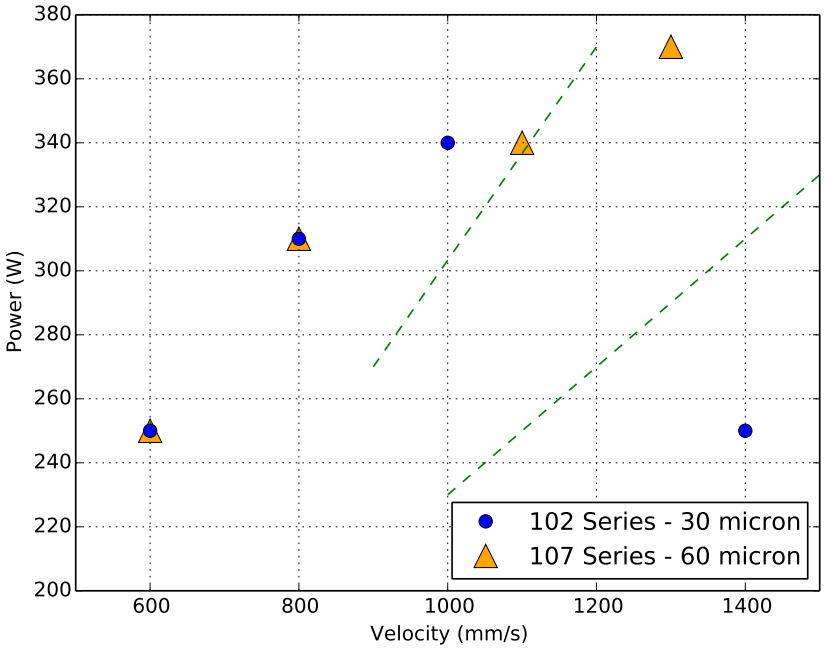

Figure 5: P-V conditions for the layer thickness study encompassing the 102 and 107 series

killer defect size (100 μm) than the 60 μm layer thickness (440 μm) in terms of the square root of the Murakami effective area ($\sqrt{area}$). The distribution of defect sizes is also significantly narrower in the 30 μm layer thickness population than the 60 μm layer thickness population. The 30 μm layer thickness population has a 25 μm standard deviation while the 60 μm layer thickness population has a standard deviation of 117 μm. These trends in killer defect size distribution also hold for the 310 W, 800 mm/s build condition, although the sizes of the defects themselves are smaller.

As before, a CDF can be used to describe the nature of the killer defects in both the 102 and 107 series in order to identify relationships between layer thickness and defect size, as well as defect size and fatigue behavior. Two such CDF plots for the smaller layer thickness 102 series and larger 107 series layer thickness are shown in Figure 8. As can be seen in this figure, the 60 μm layer

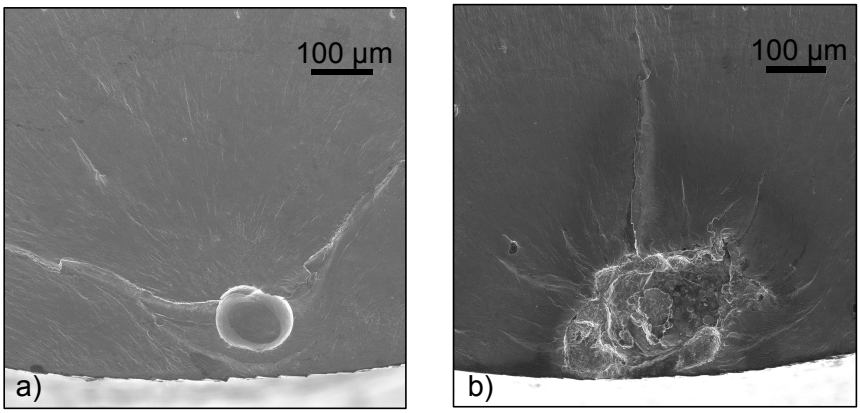

Figure 6: Representative micrographs for a) the 30 μm layer thickness 102 series showing a keyhole defect and b) the 60 μm layer thickness 107 series showing a lack of fusion defect

thickness has both significantly larger killer defects - up to nearly 700 μm in $\sqrt{area}$, and a much wider distribution of sizes than the 30 μm layer thickness specimens. Generally, the specimens built with greater laser power have killer defects that are smaller in size and have a narrower size distribution. This is consistent with the findings in the 100 and 136 series. Notably, by holding layer thickness constant at 30 μm, power and velocity conditions do not have a dramatic effect on defect size and distribution, with the exception of the 250 W-1400 mm/s condition. This is mainly due to the formation of lack of fusion defects during this build condition, which are relatively larger in size.

This data can be used as before to determine how these defects affect fatigue behavior. In Figure 9, a series of four S-N curves are shown for the 102 and 107 series. It is clear from this plot that not only does a larger build layer thickness yield larger defects when other build parameters are held constant, but that these defects, as expected, have a significant detrimental effect on fatigue life. A 60 μm layer thickness combined with a 250 W low power build condition yields poor fatigue performance, with lifetimes on the order of 10^6 cycles at stress amplitudes between 60 and 70 MPa. The CDF plots can be used to qualitatively compare fatigue performance, as, for the four build conditions in Figure 9, better fatigue performance is correlated with a narrow distribution

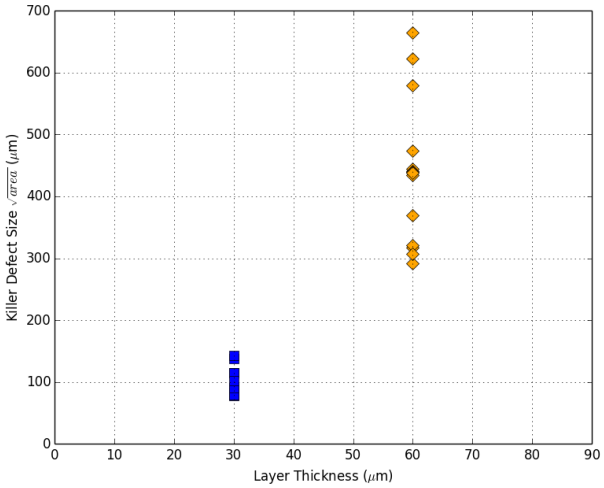

Figure 7: Distribution of killer defect sizes in the 30 and 60 μm layer thickness USF specimens for the 250 W, 600 mm/s build condition

of smaller defects that lie farther to the left in each plot of Figure 8. There is also evidence that, for the larger layer thickness, there is significantly more dependence on P-V condition in regard to defect size.

4. Discussion

Analysis based on Murakami's Equation

By controlling the size of defects through defect tolerant fatigue design within a component, it is possible to improve fatigue strength. This defect tolerant fatigue approach assumes that defects can be effectively treated as cracks. Murakami has demonstrated that small, non-propagating cracks are always found at the tips of defects and that the fatigue limit, σ_w, can be described as a threshold stress level at which these cracks will not propagate. The maximum value

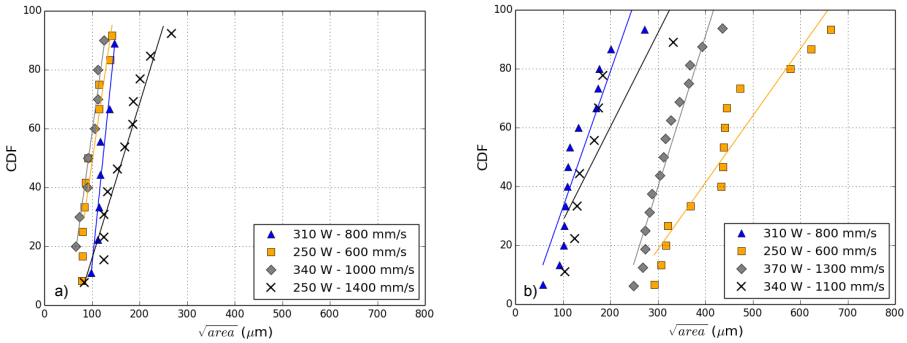

Figure 8: Cumulative distribution functions for the a) 30 μm layer thickness 102 series and b) 60 μm layer thickness 107 series

of the cyclic stress intensity factor (SIF) of a surface/near surface defect with a small edge crack is described by Murakami as:

$$\Delta K = 0.65\Delta\sigma\sqrt{\pi\sqrt{area}} \tag{2}$$

In this equation, ΔK is the SIF, $\Delta\sigma$ is the applied stress range, and $\sqrt{area}$ is the square root of the effective Murakami area parameter[21]. Below a certain size, the threshold stress intensity factor ΔK_{th} below which a crack will not propagate is determined by two parameters, $\sqrt{area}$ and the Vickers hardness HV. If $\sqrt{area}$ is in microns and the HV is in kgf/mm^2, then ΔK_{th} in MPa$\sqrt{m}$ for a surface defect is given by:

$$\Delta K_{th} = 3.3 * 10^{-3}(HV + 120)(\sqrt{area})^{1/3} \tag{3}$$

This analysis based on Murakami's equation is valid only for defects in a certain size range. There exist upper and lower bounds, beyond which the $\sqrt{area}$ model is no longer applicable, that have been well characterized in steel.[22–24] Above the upper bound in the long crack regime, the threshold stress intensity factor ΔK_{th} is invariant with defect size. The upper bound transition in steels, above which a long crack regime takes hold, is found to occur at a smaller $\sqrt{area}$ with increasing hardness. This is likely due to ΔK_{th} for long cracks in

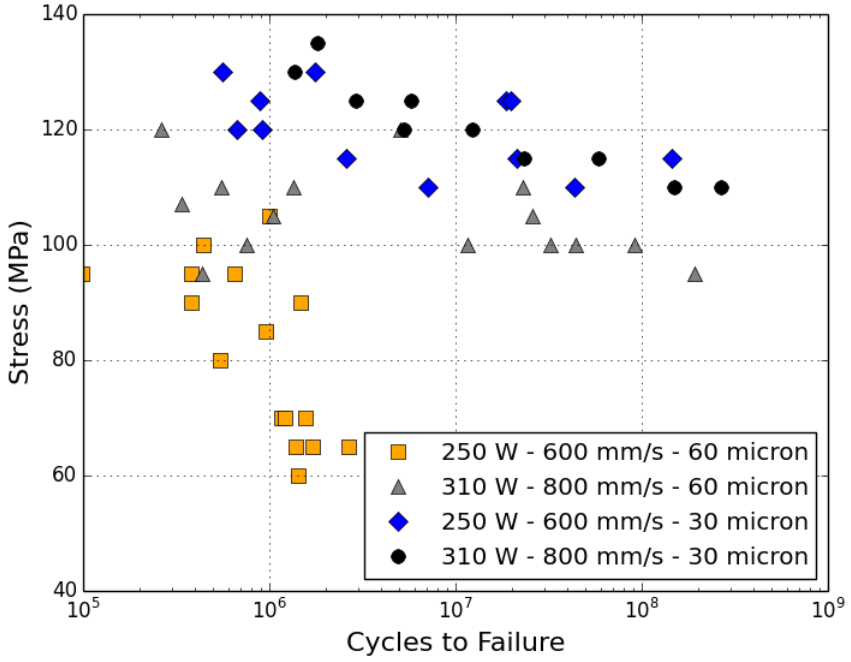

Figure 9: S-N data points for the 102 and 107 series

hard steels being lower than for soft steels because of a decreased crack closure effect.[24] As the AM AlSi10Mg considered in this work has a comparatively lower yield strength than steels, it is expected that the crack closure effect will be more pronounced and therefore the transition to a long crack regime will occur at relatively larger defect sizes.

A plot showing ΔK and ΔK_{th} as a function of $\sqrt{area}$ is shown in Figure 10. In this plot, the ΔK values for killer surface defects from this work are shown as blue circles, calculated according to Equation 2. These points represent the value of the applied SIF for a given test, calculated from the defect size revealed by fractography. The green triangles represent the ΔK_{th} points compiled from many sources in the literature[25–32] by Romano et al.[33] for additively manufactured and cast AlSi10Mg.

As the blue points represent an applied ΔK rather than a threshold ΔK_{th},

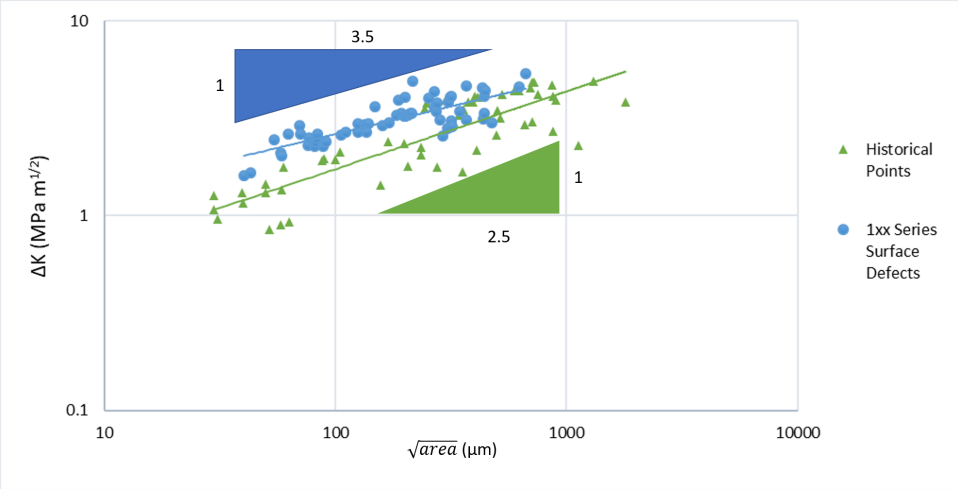

Figure 10: ΔK as a function of $\sqrt{area}$.[33]

it is not surprising that these points lie above the threshold values found in the literature. However, it should be noted that many of these tests proceeded from runouts at lower stresses close to the failure stress, suggesting that the applied ΔK should be relatively close in value to ΔK_{th}. This is apparent in Figure 10. It is also illustrative to compare the slopes of the different datasets in this plot. Based on the work of Murakami, it is expected that:

$$\Delta K_{th} = C(\sqrt{area})^{1/n} \tag{4}$$

Where C and n are constants and n≈3 within the Murakami regime. For the green triangles representing the accumulated work in the literature on AlSi10Mg, the slope of these points is approximately 0.4, resulting in an n value of 2.5 in Equation 4. It is important to note that these points represent a wide variety of build parameters, heat treatments, and post-processing conditions. Therefore, one should exercise some caution in fitting a trendline through these points. In contrast, the blue circles representing the ΔK values in Figure 10 from the present study do not vary in heat treatment or in post-processing condition. It is apparent from the plot that the slope of the line through the 1xx series points is less steep than what was found in aggregating the points from the

literature. The slope through these points is 0.28, yielding a n value of 3.5 for the AlSi10Mg specimens containing surface defects in this work. In Equation 4, it is expected that n=3 in the Murakami regime for predicting the ΔK_{th}. The literature data used here and the data from the present work lie on either side of that value but do not differ significantly. It is therefore reasonable to conclude from Figure 10 that Equation 3 is valid for defects of intermediate size in AM AlSi10Mg (100-1000 μm in $\sqrt{area}$).

As the size of defects increases further, it is expected that there will eventually be a transition to a long crack regime, as has been observed in other materials.[24] In this regime, the slope of the ΔK_{th} vs. $\sqrt{area}$ line will flatten and n will approach infinity. The data points collected in the present study may start to approach this regime, as the 3.5 n value is larger than what would be predicted from a pure analysis based on Murakami's equations. This initial analysis suggests that treating this data with a long crack model is not a valid framework for fatigue analysis in AM AlSi10Mg and using the Murakami approach is better. Only at very large defect sizes more than 1 mm in $\sqrt{area}$ is it expected to observe this transition, but this remains to be experimentally determined. As mentioned previously, this relatively large transition defect size may be due in part to the low hardness of this material.

If Equations 2 and 3 are combined and the cyclic stress range $\Delta\sigma$ is taken as $2\sigma_w$, an expression for the fatigue limit σ_w can be determined:

$$\sigma_w = \frac{1.43(HV + 120)}{(\sqrt{area})^{1/6}} \tag{5}$$

Note that this equation is valid only for surface cracks and there is a different prefactor if interior cracks are considered. While this equation has most commonly been used to predict the fatigue limit in steels, there exists past work in which this equation has been extended to aluminum. Murakami proposes an unmodified version of Equation 5 and successfully applies it to a 2017-T4 alloy.[21] Recently, more extensive work has shown that a modified version of this equation can be used to determine fatigue limits for cast aluminum alloy A356,

in which the 120 value is changed to 75.[34] The dependencies of Equation 5 are therefore valid, but the exact values are subject to modification, for aluminum alloys. Like ΔK_{th}, the fatigue limit σ_w in MPa is also determined by two parameters, the Vickers hardness in kgf/mm^2 and $\sqrt{area}$ in μm. Above this size, in the long-crack regime, an invariant ΔK_{th} can be assumed and a long crack regime can be used to determine fatigue behavior. Below this limit, ΔK_{th} varies with defect size due to reduced crack closure effects resulting from the limited wake of these small cracks. Equation 3 can be rearranged to find the point at which this transition occurs:

$$\sqrt{area}_{trans} = (\frac{\Delta K_{th,lc}}{3.3 * 10^{-3}(HV + 120)})^3 \tag{6}$$

The value of this transition size in μm is therefore dependent on the long crack threshold SIF, $\Delta K_{th,lc}$ in MPa$\sqrt{m}$, which is a constant material property, and the Vickers hardness, HV in kgf/mm^2. Immediately below this transition size, the fatigue limit can be determined from the Murakami-based Equation 5. Immediately above this transition size, the fatigue limit stress amplitude in the presence of large defects, $\sigma_{w,ld}$, is determined according to:

$$\sigma_{w,ld} = \frac{434 * \Delta K_{th,lc}}{(\sqrt{area})^{1/2}} \tag{7}$$

This expression is generated from Equation 2, substituting $\Delta K_{th,lc}$ for ΔK and $2\sigma_{w,ld}$ for $\Delta\sigma$. On a double logarithmic plot, there is therefore a change in slope from -1/6 to -1/2 at $\sqrt{area}_{trans}$. However, dividing the fatigue strength dependence into two regimes alone is incomplete as there is a critical defect size below which defects can be considered non-detrimental and which is not captured by Murakami theory. Equation 6 can be modified to estimate the lower bound of defect size at which the size-dependent Murakami $\sqrt{area}$ parameter is no longer a valid means of calculating the fatigue limit of a material.[24] This bound in terms of critical size is determined by the effective threshold SIF range, $\Delta K_{eff,th}$ in a similar fashion to Equation 6:

$$\sqrt{area}_{critical} = (\frac{\Delta K_{eff,th}}{3.3 * 10^{-3}(HV + 120)})^3 \quad (8)$$

Fatigue Limit as a Function of Defect Size

While Vickers hardness is easily measured, it is relatively difficult to obtain values for $\Delta K_{eff,th}$ experimentally, especially in aluminum alloys. As such, the endurance limit of aluminum alloys in the very short crack regime will not be considered here.

Having established Equation 5 and 7, it is possible to interpret the data collected in this work in the light of the two different fatigue limit regimes. The first regime is a size-dependent regime in which the Murakami model of non-propagating cracks dominates. At larger crack sizes, a long crack regime takes hold and Equation 7 can be used to calculate the fatigue limit.

The average Vickers hardness measurements for the different groupings of specimens are shown in Tables 3 and 4.

	100-1	100-2	100-4	136-1	136-2	136-4	136-10
HV	142	136	127	137	134	130	140

Table 3: Vickers hardness measurements for 100 and 136 Series

	102-1	102-2	102-3	102-4	107-1	107-2	107-3	107-4
HV	125	122	122	137	136	130	131	140

Table 4: Vickers hardness measurements for 102 and 107 Series

From Tables 3 and 4, it is found that the average Vickers hardness across all of the specimens is 130 with a standard deviation of 7. Therefore, the hardness-dependent equations above should use a value within this range in order to determine the bounds of the different fatigue limit regimes.

As crack growth was not monitored directly, the experiments conducted in this work did not explicitly obtain a value for $\Delta K_{th,lc}$. Past work has demon-

strated that $\Delta K_{th,lc}$ is approximately 3 MPa$\sqrt{m}$ in cast AlSi11 and approxi-
330 mately 3.6 MPa$\sqrt{m}$ in AlSi7Mg at R=-1.[35,36] It is expected that this will not vary significantly with differing R ratios and so bounds of 3 and 4 MPa$\sqrt{m}$ were established for $\Delta K_{th,lc}$ in this optimization analysis. The total data for all the tests that were either runout to $>10^7$ cycles or tested to failure are shown in Figure 11. The runouts are denoted by red circles and the tests completed
335 to failure are denoted by green squares. It is expected that the runout tests reside beneath the fatigue limit and that failed tests reside above the fatigue limit. All runout tests had their cyclic stress amplitudes increased such that they eventually failed. Therefore, the killer defect size of both runout tests and tests that were completed to failure can be found.

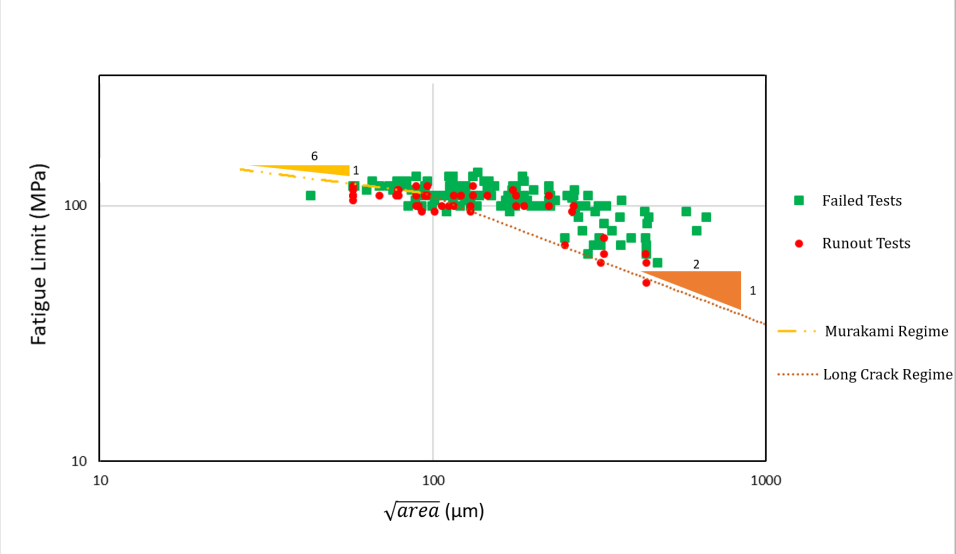

Figure 11: Discrete Kitagawa Diagram showing fatigue limit as a function of $\sqrt{area}$. Different size-dependent regimes are indicated by the different lines.

340 By dividing the dataset into two distinct regimes according to Equations 5 and 7, the lines in Figure 11 can be optimized such that the number of failed tests above and runout tests below the fatigue limit line is maximized. This has been done with an evolutionary algorithm. Because of the overestimation of the

fatigue limit, a scaling factor was also applied to the equations governing the three regimes as a part of this optimization. For each step in the evolutionary algorithm, this scaling factor and $\Delta K_{th,lc}$ were allowed to vary while all other parameters were held constant until optimized values were found. The optimal scaling factor to fit the data to the three regimes described above is 0.67.

The first regime (Murakami) is where the dependence of the fatigue limit on defect size begins. In this evolutionary optimization, it is found that this domain of this regime is relatively small, from 26 to 93 μm in $\sqrt{area}$. This stands in contrast to some past work on lower hardness materials and the ΔK_{th} analysis of Figure 10, in which this regime extends into the 100s of μm.[33] There are a few reasons behind this discrepancy. In the Kitagawa optimization of Figure 11, the runout data is included which biases the optimal slope lower, increasing the domain of the long crack regime and decreasing the value of $\sqrt{area}_{trans}$. It is notable that by fitting this long crack regime line, the hardness and $\sqrt{area}_{trans}$ values can be used to calculate $\Delta K_{th,lc}$ according to Equation 6. For this fit, a $\Delta K_{th,lc}$ value of 3.74 MPa $\sqrt{m}$ is obtained, which is relatively close to the values obtained in AlSi11 and AlSi7Mg by Stanzl-Tschegg, et al.[35,36] Ultimately, this optimization analysis results in 80% of the data points in Figure 10 being correctly binned above or below the fatigue limit. If only the Murakami equation is employed, the largest this value reaches is 57%, suggesting that a long crack regime is an appropriate model for defects with 93 μm in $\sqrt{area}$ and above.

5. Conclusions

The fatigue behavior of AM AlSi10Mg was investigated for different build parameter conditions in the context of a defect-driven Murakami model. It was found that:

1) In the 220-370 W range, higher laser power decreases the size of killer defects. These smaller killer defects in turn affect the fatigue behavior, significantly increasing lifetime.

2) Of the build parameters considered, layer thickness during fabrication is

the largest driver of defect size and distribution. Smaller layer thickness yields improved fatigue performance at a given stress level.

3) Plotting ΔK as a function of $\sqrt{area}$ for all killer surface defects observed yields good agreement with data from the literature and suggests that Equation 4 can be used to model ΔK.

4) Extending a two-regime model to all data points, including runout tests, suggests that a long crack regime dominates for defects above 93 μm in $\sqrt{area}$.

6. Acknowledgements

We would like to thank Bernd Schönbauer for useful discussions. The authors would also like to acknowledge funding through CEED-17-0026.

References

[1] Buchbinder D, Meiners W, Wissenbach K, Poprawe R. Selective laser melting of aluminum die-cast alloy—correlations between process parameters, solidification conditions, and resulting mechanical properties. *J Laser Appl.* 2015;27(S2):S29205.

[2] Scott-Emuakpor O, Schwartz J, George T, Holycross C, Cross C, Slater J. Bending fatigue life characterisation of direct metal laser sintering nickel alloy 718. *Fatigue Fract Eng Mater Struct.* 2015;38(9):1105–1117.

[3] Thijs L, Verhaeghe F, Craeghs T, Humbeeck J, Kruth JP. A study of the microstructural evolution during selective laser melting of Ti-6Al-4V. *Acta Mater.* 2010;58:3303–3312.

[4] Sun P, Fang ZZ, Xia Y, Zhang Y, Zhou C. A novel method for production of spherical Ti-6Al-4V powder for additive manufacturing. *Powder Technol.* 2016;301:331–335.

[5] Read N, Wang W, Essa K, Atallah MM. Selective laser melting of AlSi10Mg alloy: Process optimisation and mechanical properties development. *Materials and Design.* 2015;65:417–424.

[6] Trevisan F, Calignano F, Lorusso M, et al. On the selective laser melting (slm) of the AlSi10Mg alloy: Process, microstructure, and mechanical properties. *Mater.* 2017;10(1):76.

[7] Herzog D, Seyda V, Wycisk E, Emmelmann C. Additive manufacturing of metals. *Acta Mater.* 2016;117:371–392.

[8] Elzanaty H. Effect of composition on the microstructure, tensile and hardness properties of Al-xSi alloys. *J Mater Sci Surf Eng.* 2015;2:126–129.

[9] Kempen K, Thijs L, Humbeeck JV, Kruth JP. Processing AlSi10Mg by selective laser melting: parameter optimisation and material characterisation. *Mater Sci Technol.* 2015;31(8):917–923.

[10] Wei H, Elmer J, DebRoy T. Three-dimensional modeling of grain structure evolution during welding of an aluminum alloy. *Acta Mater.* 2017;126:413–425.

[11] Aboulkhair NT, Everitt NM, Ashcroft I, Tuck C. Reducing porosity in AlSi10Mg parts processed by selective laser melting. *Addit Manuf.* 2014; 1-4:77–86.

[12] Yadollahi A, Shamsaei N. Additive manufacturing of fatigue resistant materials: Challenges and opportunities. *Int J Fatigue.* 2017;98:14–31.

[13] Fatemi SA, Ashany JZ, Aghchai AJ, Abolghasemi A. Experimental investigation of process parameters on layer thickness and density in direct metal laser sintering: a response surface methodology approach. *Virtual and Physical Prototyping.* 2017;12(2):133–140.

[14] Wycisk E, Solbach A, Siddique S, Herzog D, Walther F, Emmelmann C. Effects of defects in laser additive manufactured Ti-6Al-4V on fatigue properties. *Phys Proc.* 2014;56:371–378.

[15] Kempen K, Thijs L, Humbeeck JV, Kruth JP. Mechanical properties of AlSi10Mg produced by selective laser melting. *Phys Proc.* 2012;39:439–446.

[16] Brandl E, Heckenberger U, Holzinger V, Buchbinder D. Additive manufactured AlSi10Mg samples using selective laser melting: Microstructure, high cycle fatigue, and fracture behavior. *Mater Des*. 2012;34:159–169.

[17] Mayer H. Recent developments in ultrasonic fatigue. *Fatigue Fract Eng Mater Struct*. 2016;39(1):3–29.

[18] Biffi C, Fiocchi J, Bassani P, et al. Microstructure and preliminary fatigue analysis on AlSi10Mg samples manufactured by SLM. *Procedia Struct Integrity*. 2017;7:50–57.

[19] Mayer H. Fatigue crack growth and threshold measurements at very high frequencies. *Int Mater Rev*. 1999;44(1):1–34.

[20] Murakami Y, Kodama S, Konuma S. Quantitative evaluation of effects of nonmetallic inclusions on fatigue strength of high strength steel. *Trans Jpn Soc Mech Eng*. 1988;54:688–695.

[21] Murakami Y. *Metal Fatigue: Effects of Small Defects and Nonmetallic Inclusions*. Elsevier. 2002.

[22] Chapetti MD. A simple model to predict the very high cycle fatigue resistance of steels. *Int J Fatigue*. 2011;33(7):833–841.

[23] Schönbauer BM, Yanase K, Endo M. The influence of various types of small defects on the fatigue limit of precipitation-hardened 17-4PH stainless steel. *Theor Appl Fract Mech*. 2017;87:35–49.

[24] Schönbauer BM, Mayer H. Effect of small defects on the fatigue strength of martensitic stainless steels. *Int J Fatigue*. 2019;127:362–375.

[25] Beretta S. Fatigue strength assessment of AlSi7Mg castings. In *Proc Int Conf Importance Fatigue Process*. Balkema Publishers; 1999.

[26] Oberwinkler C, Leitner H, Eichlseder W. Computation of fatigue safety factors for high-pressure die cast (HPDC) aluminum components taking into account the pore size distribution. *SAE Technical Paper*;1999.

[27] Nadot Y, Mendez J, Ranganathan N. Influence of casting defects on the fatigue limit of nodular cast iron. *Int J Fatigue*. 2004;26(3):311–319.

[28] Houria MI, Nadot Y, Fathallah R, Roy M, Maijer DM. Influence of casting defect and SDAS on the multiaxial fatigue behaviour of A356-T6 alloy including mean stress effect. *Int J Fatigue*. 2015;80:90–102.

[29] McDowell D, Gall K, Horstemeyer M, Fan J. Microstructure-based fatigue modeling of cast A356-T6 alloy. *Eng Fract Mech*. 2003;70(1):49–80.

[30] Linder J, Axelsson M, Nilsson H. The influence of porosity on the fatigue life for sand and permanent mould cast aluminium. *Int J Fatigue*. 2006; 28(12):1752–1758.

[31] Roy M, Nadot Y, Maijer DM, Benoit G. Multiaxial fatigue behaviour of A356-T6. *Fatigue Fract Eng Mater Struct*. 2012;35(12):1148–1159.

[32] Ceschini L, Morri A, Sambogna G. The effect of hot isostatic pressing on the fatigue behaviour of sand-cast A356-T6 and A204-T6 aluminum alloys. *J Mater Process Technol*. 2008;204(1):231–238.

[33] Beretta S, Romano S. A comparison of fatigue strength sensitivity to defects for materials manufactured by am or traditional processes. *Int J Fatigue*. 2017;94:178–191.

[34] Tajiri A, Nozaki T, Uematsu Y, et al. Fatigue limit prediction of large scale cast aluminum alloy A356. *Procedia Mater Sci*. 2014;3:924–929. 20th European Conference on Fracture.

[35] Stanzl-Tschegg S, Mayer H, Tschegg E, Beste A. In-service loading of AlSi11 aluminium cast alloy in the very high cycle regime. *Int J Fatigue*. 1993;15(4):311–316.

[36] Stanzl-Tschegg S, Mayer H, Beste A, Kroll S. Fatigue and fatigue crack propagation in AlSi7Mg cast alloys under in-service loading conditions. *Int J Fatigue*. 1995;17(2):149–155.